JOURNAL OF SPACECRAFT AND ROCKETS
Vol. 36, No. 3, May–June 1999

Mars Pathfinder Entry Temperature Data, Aerothermal Heating, and Heatshield Material Response

Frank S. Milos* and Y.-K. Chen†
NASA Ames Research Center, Moffett Field, California 94035-1000
William M. Congdon‡
Applied Research Associates, Inc., Littleton, Colorado 80123
and
Janine M. Thornton§
Lockheed Martin Astronautics, Denver, Colorado 80201

The Mars Pathfinder probe contained instrumentation that measured heatshield temperatures during entry. A description of the experiment, the data, and an analysis of the entry environment and material response are presented. Navier–Stokes forebody heating calculations show a peak unblown radiative-equilibrium heat flux of 118 W/cm^2 at the stagnation point and 120 W/cm^2 on the shoulder for turbulent flow. The heat load is 3.8 kJ/cm^2 on the nose, decreases along the frustum, then increases to 2.7–3.1 kJ/cm^2 on the shoulder depending on the onset time for turbulence. One-dimensional charring material response is calculated using three different models. Stagnation-point temperature data are consistent with about 85% of fully catalytic laminar heating. Shoulder temperature data are inconclusive, but are consistent with fully catalytic laminar heating or with 85% of fully catalytic heating with early onset of turbulence. Aft temperature data indicate a peak heat flux and heat load of about 1.3 W/cm^2 and 70 J/cm^2, respectively. The aft heating profile is about 20 s longer than the forebody heating profile. Bondline temperature data, although not useful for quantitative analysis of aerothermal heating, clearly show the heatshield had adequate thickness margins for the actual entry.

Nomenclature

B' = dimensionless surface blowing rate
C_H = heat transfer coefficient, kg/m^2-s
c = molar density, kmol/m^3
D = vehicle diameter, m
D_{ij} = diffusion coefficient, m^2/s
H_R = total recovery enthalpy, J/kg
h = enthalpy, J/kg
j = diffusive mass flux, kg/m^2-s
k = thermal conductivity, W/m-K
M = molecular weight, kg/kmol
$\dot{m}$ = surface blowing rate, kg/m^2-s
P = pressure, N/m^2
q = surface heat flux, W/m^2
R = gas constant, J/kmol-K
Re_∞ = flight Reynolds number, $(\rho u/\mu)_\infty D$
r = radial coordinate, m
S = streamlength from front centerline, m
T = temperature, K
v = surface-normal velocity, m/s
x = mole fraction
y = mass fraction
y^+ = inner-region coordinate, $\eta\sqrt{(\rho_w \tau_w)}/\mu_{1w}$
α = surface absorptivity
β = ballistic coefficient, kg/m^2
γ = reaction efficiency
ε = surface emissivity
η = coordinate normal to surface, m
κ = von Kármán constant
λ = blowing reduction parameter
μ = viscosity, kg/m-s
ρ = density, kg/m^3
σ = Stefan–Boltzmann constant, W/m^2-K^4
ω = surface reaction rate, kmol/m^2-s
ϖ = vorticity, 1/s

Subscripts

c = char
cond = conduction
g = pyrolysis gas
i, j = species
RE = radiative equilibrium
r = reaction
rad = radiation
s = surface adsorbed species or adsorption site
T = translation
t = turbulent
V = vibration
w = material surface
1 = unblown
∞ = freestream

Received March 15, 1998; presented as Paper 98-2681 at the AIAA/ASME 7th Joint Thermophysics and Heat Transfer Conference, Albuquerque, NM, June 15–18, 1998; revision received Aug. 15, 1998; accepted for publication Feb. 22, 1999.

*Aerospace Engineer, Thermal Protection Materials and Systems Branch, MS 234-1. Senior Member AIAA.
†Aerospace Engineer, Thermal Protection Materials and Systems Branch.
‡Research Scientist. Member AIAA.
§Senior Engineer.

Introduction

ON July 4, 1997, the Mars Pathfinder probe entered and traversed the atmosphere of Mars and successfully landed on the surface. Figure 1 shows the aeroshell geometry. The Pathfinder vehicle was an axisymmetric 70.2-deg half-angle blunted cone with a rounded shoulder and a truncated 46.6-deg conical backshell. The nose, shoulder, and vertical-backplate radii were 0.6638, 0.0662, and about 0.297 m, respectively. The overall diameter and length were 2.65 and 1.5 m, respectively.

The heatshield material on the forebody and shoulder was a low-density ablator, called Super-Light Ablator (SLA)-561V, with nominal thickness of 1.90 cm (Ref. 1). This material consists of a fiberglass phenolic honeycomb with about 1-cm cells that are packed

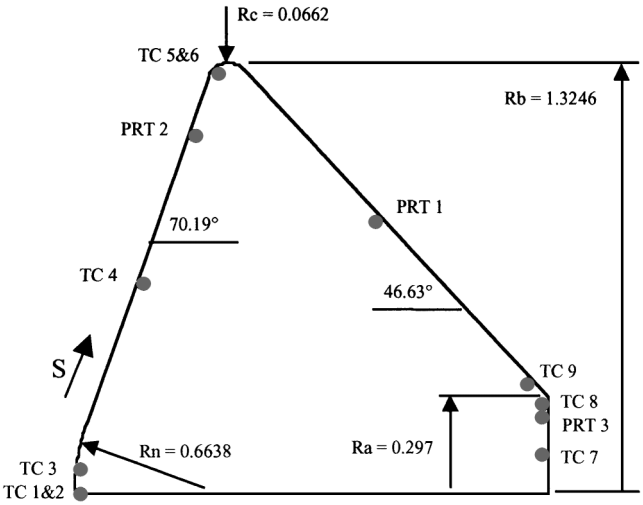

Fig. 1 Pathfinder geometry showing locations of TCs 1–9 and resistance thermometers PRT1–PRT3; sensors are not coplanar.

with a charring ablative compound containing elastomeric silicone and various fillers.[2] The conical backshell was covered with a spray-on version of the same ablative compound, called SLA-561S, with nominal thickness of 0.48 cm. The backplate and a small part of the aft conical frustum were covered with silicone-impregnated reusable ceramic ablator (SIRCA) tiles, which varied in thickness from 0.48 to 1.2 cm depending on location.[3] Most of the aeroshell structure was aluminum honeycomb sandwiched between graphite polyimide faceplates, but in some sections the honeycomb was filled to provide greater stiffness and machinability. The SIRCA tiles were bonded to an aluminum backshell that was bolted to the primary structure.

Several studies were conducted to determine the aerothermal heating and thermal protection system (TPS) sizing for Pathfinder.[4–6] Most studies used a ballistic coefficient $\beta = 55$ kg/m^2, but the actual value was 63 kg/m^2 corresponding to an entry mass of 585.3 kg (Ref. 7). For the forebody, the most detailed study was provided by Chen et al.,[4] who performed quasisteady laminar Navier–Stokes calculations at 21 trajectory points coupled with transient surface temperatures and species blowing rates provided by a one-dimensional material response code at each surface node. Using a fully catalytic surface and the highest heat load (shallowest) trajectory, the minimum TPS thickness required to maintain a bondline temperature of 520 K was under 1.4 cm on the forebody and around the shoulder. The final design thickness of 1.9 cm accounted for the increase in β (assuming the flow is laminar) and included about 20% margin.

The increased value of β causes faster descent through the Martian atmosphere and increases the probability of turbulent heating on the frustum. Mitcheltree[8] calculated unblown laminar and turbulent flow solutions using a shallow entry, $\beta = 60$ kg/m^2, and transition criterion equivalent to $Re_\infty = 9 \times 10^5$. Turbulence greatly increased the predicted heating along the entire forebody frustum, but transition was predicted not to occur until 10 s after peak nosetip heating. The peak heating rate and heat load on the frustum were comparable to the laminar stagnation-point values. These results suggested that the constant-thickness forebody heatshield design with added margin, derived from laminar stagnation-point heating, could be adequate to survive the occurrence of turbulent flow.

For the Pathfinder afterbody heatshield design, Navier–Stokes wake flowfield solutions were calculated by Mitcheltree and Gnoffo[9] and by Hass and Venkatapathy.[10] These two studies considered two and four trajectory times, respectively, for different trajectories based on a ballistic coefficient of 55 kg/m^2. Both studies predicted maximum afterbody heating on the vertical backplate and significantly lower heating along the afterbody frustum. The peak heating rate on the backplate was only 8–10 W/cm^2, which was about 5–7% of peak forebody stagnation-point heating. The peak backshell heating was 10–40% of the backplate heating depending on location.

The afterbody heating history and heat load are difficult to estimate because of the small number of trajectory times considered. The general design methodology is to scale the forebody heating based on a small number of wake flowfield solutions, then to add a very large safety margin (100–200%) to the maximum scaled heat load to determine the required TPS thickness. This degree of conservatism is warranted. Olynick et al.[11] computed afterbody flowfields at 11 trajectory points for the Stardust vehicle, which has a similar biconic shape but with shallower frustum angles. Their study also found maximum heating on the vertical backplate, but the afterbody heating profiles had significantly longer duration than the forebody heating profiles. Thus, simple scaling of the forebody heating profile based on one or two wake flowfield solutions could result in gross underprediction of afterbody heat loads.

The Mars Pathfinder aeroshell contained several thermocouples and thermometers that provided temperature data during the hypersonic entry. This work will describe the experiment and the data, and then present an analysis of the entry aerothermal environment and the heatshield material response. The purpose of the analysis is to determine if the temperature data provide information on actual heating environments in comparison with the predictions.

Temperature Instrumentation and Data Reduction

As shown in Fig. 1, the aeroshell contained nine type-K thermocouples (TC1–TC9) and three platinum resistance thermometers (PRT1–PRT3). The TCs used thin wires installed parallel to the surface to minimize temperature lag and heat conduction down the TC wires. The PRTs were small platinum/ceramic devices ($4 \times 4 \times 1$ mm) with a relatively fast thermal response time.

TC1–TC3 were near the forebody nose at different depths, TC4 was at the bondline about halfway along the forebody frustum, TC5 and TC6 were on the shoulder at different depths, and TC7–TC9 were just below the surface of the SIRCA tiles.[1,3] PRT1 was at the bondline about halfway along the backshell frustum, and the other two PRTs were attached to fore and aft aluminum blocks inside the structure. These aluminum blocks served as isothermal reference junctions for the nine TCs. The various sensors were not coplanar; however, the vehicle was spin stabilized (2 rpm) and remained at low angle of attack (under 5 deg) (Refs. 7 and 12); thus the flowfield and material response are considered to be axisymmetric. Instrument locations and depths are listed in Table 1. The materials and thicknesses at the TC locations are given in Table 2.

In this work, time zero for atmospheric entry is considered to be 900 s after separation of the Mars Pathfinder entry probe from the cruise stage. At time zero, the probe velocity, the entry angle, the altitude, and the atmospheric pressure were 7483 m/s, −13.65 deg, 133.3 km, and 1×10^{-9} bar, respectively.[7] During entry, voltage measurements from each TC and resistance thermometer were taken at a variable rate that increased from 0.125 Hz initially to 1 Hz at 78 s. The PRT voltages were converted to resistance using linear calibration lines, then resistance was converted to temperature using cubic calibration functions.[13] The TC (hot-junction) voltages must be added to the reference (cold-junction) voltages before the thermocouple temperature can be deduced. Thus, the cold-junction temperature (as measured by the PRT attached to the aluminum block) was converted back to voltage using a cubic function, this

Table 1 Instrument locations and depths

Instrument	r, cm	S, cm	Depth, cm
T1	0.00	0.00	0.400
T2	0.00	0.00	0.953
T3	7.62	7.64	1.905
T4	66.44	69.7	1.905
T5	130.4	138.0	0.953
T6	130.4	138.0	1.905
T7	12.0		0.038
T8	27.6		0.038
T9	34.0		0.038
PRT1	83.9	212.5	1.340
PRT2	110.0	(inside structure)	
PRT3	23.5	(inside structure)	

voltage was added to the thermocouple voltage, and the voltage sum was converted to the hot-junction temperature using a cubic calibration curve.[13]

The voltage data were transmitted to Earth and reduced to temperature vs time data, presented in Table 3. Nominal data uncertainty is ±2.2 K with exceptions to be described. TC1, TC7, and TC8 are not included in Table 3 because they did not provide any usable data. Examination of in-flight vehicle health check data suggests these three thermocouples failed prior to the first health check, i.e., before or during launch, because these TCs showed no sensitivity to the vehicle's orientation or distance to the sun. The other six TCs and PRT1 measured an increase in temperature because of aerothermal heating of the vehicle surface. PRT3, which was attached to a 29-g aluminum block inside the structure, showed no significant temperature change, as expected. PRT2, which was attached to a 38-g aluminum block inside the structure, showed a constant temperature of 233.3 K throughout entry.

Table 2 Materials and thicknesses

Material	Thickness, cm
Nosetip and midfrustum (T2–T4)	
SLA-561V heatshield	1.905
Polyimide faceplate	0.038
Aluminum honeycomb	3.175
Polyimide faceplate	0.038
Shoulder (T5 and T6)	
SLA-561V heatshield	1.340
Polyimide faceplate	0.038
Aluminum honeycomb (filled)	5.715
Backshell (PRT1)	
SLA-561S heatshield	0.483
Polyimide faceplate	0.038
Aluminum honeycomb	1.270
Polyimide faceplate	0.038
Backplate (T9)	
SIRCA 15-F heatshield	1.035
RTV-560	0.015
Aluminum	0.400

The PRT2 data are incorrect because the measurements are pegged at the low-temperature cutoff of the calibration curve. PRT1 is similarly pegged at 231.2 K for the first 26 data points in Table 3. Therefore, the forebody temperature data for TCs 2–6 are incorrect because the pegged cold-junction temperature for PRT2 was used in the data reduction. The actual TC temperatures are lower than indicated in Table 3. The error is equal to the difference between the pegged PRT2 temperature of 233.3 and the actual isothermal block temperature.

The data can be corrected using results from the solar thermal vacuum (STV) tests[14] that were conducted prior to launch to determine the vehicle temperature distribution at different times during the interplanetary cruise. One STV condition, which simulated 41-deg off-sun attitude at 1.55 AU (2.32×10^8 km from the sun), was a simulation of the vehicle temperature distribution at cruise-stage separation. Although the STV test did not exactly reach steady state near the nose, the temperature in the vicinity of PRT2 and PRT1 can be estimated at 215.3 ± 2 K and 231.2 ± 1 K, respectively. Thus, to account for pegging of PRT2, $233.3 - (215.3 \pm 2) = 18 \pm 2$ K must be subtracted from the tabulated temperatures for TCs 2–6. Similarly, to account for the apparent pegging of PRT1, up to 1 K may be subtracted from the first 26 data points.

The proposed 18 ± 2 K correction is supported by other STV data. Near the shoulder, the STV temperatures were about 224 ± 1 K and steady. The corrected initial temperature for TC5 and TC6, about

Table 3 Pathfinder temperature data

Time, s	TC2, K	TC3, K	TC4, K	TC5, K	TC6, K	TC9, K	PRT1, K	PRT3, K
2	215.5[a]	216.0[a]	218.6[a]	241.2[a]	241.9[a]	233.9[a]	231.2[b]	255.8
10	215.8	216.3	218.7	241.4	241.9	233.6	231.2	255.9
18	215.5	216.2	218.6	241.2	241.9	232.7	231.2	255.8
26	215.5	216.2	218.6	241.2	241.8	232.1	231.2	255.8
34	215.5	216.3	218.6	241.2	241.8	241.9	231.2	255.8
42	215.8	216.3	218.7	241.4	241.9	284.8	231.2	255.8
50	216.0	216.2	218.7	241.8	241.9	346.0	231.2	255.8
58	219.8	215.9	218.6	244.5	242.0	427.6	231.2	255.7
66	235.6	216.0	218.6	253.5	241.9	494.3	231.2	255.8
74	272.5	216.4	219.6	276.1	241.9	536.1	231.2	255.8
78	299.2	216.3	219.3	290.4	241.9	546.2	231.2	255.8
79	305.2	216.3	219.3	294.0	241.9	548.1	231.2	255.7
80	310.8	216.7	219.6	297.4	242.2	550.2	231.2	255.6
81	316.1	216.3	219.4	300.3	241.9	553.4	231.2	255.6
82	321.1	216.3	219.2	303.1	242.0	559.4	231.2	255.7
83	326.8	216.4	219.2	306.2	242.1	564.7	231.2	255.6
84	334.1	216.2	219.2	309.2	242.0	570.2	231.2	255.7
85	341.7	216.4	219.2	312.5	242.1	574.2	231.2	255.7
86	348.7	216.5	219.3	316.2	242.1	576.2	231.2	255.6
87	355.8	216.4	219.2	319.8	242.0	578.2	231.2	255.7
88	363.9	216.9	219.6	324.6	242.3	579.8	231.2	255.5
89	371.5	216.9	219.6	328.7	242.3	582.1	231.2	255.5
90	378.6	216.8	219.3	332.4	242.2	585.2	231.2	255.7
91	386.5	217.0	219.7	336.6	242.3	588.2	231.2	255.5
92	393.7	217.0	219.5	340.3	242.3	590.8	231.2	255.6
93	401.3	217.2	219.6	344.3	242.4	591.2	231.2	255.6
94	408.8	217.4	219.5	348.3	242.4	590.8	231.5	255.6
95	416.6	217.5	219.8	352.5	242.7	589.9	232.7	255.5
96	423.5	217.9	219.7	356.3	242.8	586.7	233.7	255.6
97	430.9	218.3	219.9	360.6	243.1	582.5	235.0	255.4
98	437.7	218.4	219.9	364.4	242.9	578.0	236.1	255.6
99	444.3	218.5	219.9	368.6	243.1	571.7	237.6	255.5
100	450.8	219.3	220.3	372.9	243.4	565.3	238.7	255.4
101	457.0	219.6	220.5	377.3	243.7	559.1	240.1	255.4
102	462.6	220.0	220.6	381.1	244.0	552.7	241.4	255.4
103	468.0	220.1	220.4	385.2	244.0	546.6	242.7	255.5
104	473.2	220.9	220.9	389.3	244.2	540.1	244.0	255.5
105	478.1	221.6	221.2	393.2	244.5	533.2	245.3	255.5
106	483.1	222.4	221.7	397.5	245.2	526.8	246.7	255.4
107	487.2	222.8	221.7	401.0	245.2	520.8	248.0	255.5
108	491.5	223.9	222.2	404.8	245.8	515.0	249.2	255.4

(Continued)

Table 3 Pathfinder temperature data (continued)

Time, s	TC2, K	TC3, K	TC4, K	TC5, K	TC6, K	TC9, K	PRT1, K	PRT3, K
109	495.1	224.3	222.3	408.2	246.0	509.5	250.4	255.5
110	498.8	225.4	223.0	411.9	246.5	503.6	251.7	255.4
111	502.0	226.1	223.4	415.3	247.0	498.6	252.8	255.4
112	505.1	226.7	223.5	418.2	247.2	494.2	254.0	255.5
113	507.7	227.7	223.9	421.3	247.4	489.3	254.9	255.4
114	510.4	228.6	224.5	424.5	248.0	484.6	255.9	255.4
115	512.8	229.3	224.9	427.4	248.3	480.3	256.9	255.4
116	515.1	230.0	225.5	430.3	248.8	475.8	258.0	255.3
117	516.8	230.4	225.5	432.6	248.8	472.2	259.0	255.4
118	518.7	231.3	226.1	435.1	249.3	468.5	259.7	255.4
119	520.1	231.7	226.4	437.5	249.5	464.8	260.6	255.5
120	521.5	232.6	227.0	439.8	250.0	460.9	261.4	255.3
121	523.0	232.9	227.5	442.3	250.1	457.4	262.3	255.3
122	523.8	233.4	227.8	443.9	250.3	454.2	262.9	255.4
123	524.9	233.9	228.2	446.1	250.7	450.7	263.7	255.3
124	525.6	234.5	228.6	447.8	250.9	448.0	264.2	255.4
125	526.6	234.8	229.3	449.8	251.3	444.7	264.9	255.3
126	527.0	235.3	229.5	451.4	251.4	441.7	265.6	255.3
127	527.1	235.8	229.7	452.6	251.5	439.2	266.0	255.4
128	527.7	236.2	230.4	454.4	252.1	436.2	266.6	255.2
129	527.6	236.3	230.3	455.5	251.9	433.3	267.3	255.3
130	527.6	236.6	230.5	456.6	252.1	431.2	267.7	255.4
131	527.7	237.2	231.0	457.9	252.3	428.6	268.1	255.3
132	527.7	237.1	231.2	459.2	252.5	425.8	268.7	255.3
133	527.4	237.3	231.3	460.0	252.6	424.1	269.0	255.4
134	527.4	237.8	231.9	461.4	253.0	421.2	269.5	255.2
135	526.9	237.9	231.7	461.9	252.9	419.4	269.9	255.4
136	526.7	238.1	232.0	462.9	253.0	416.7	270.5	255.3
137	526.1	238.8	232.3	463.6	253.4	414.7	270.7	255.2
138	525.3	238.6	232.2	464.1	253.4	412.9	271.1	255.3
139	524.9	239.1	232.5	464.8	253.6	410.7	271.5	255.2
140	524.5	239.1	232.7	465.7	253.8	408.6	271.9	255.2
141	523.7	239.5	232.8	466.0	254.0	406.7	272.2	255.2
142	523.1	239.6	233.0	466.6	254.1	404.7	272.6	255.2
143	522.1	239.8	232.8	466.8	254.1	403.0	272.8	255.2
144	521.5	239.7	233.1	467.4	254.2	401.1	273.3	255.2
145	520.7	239.8	232.9	467.7	254.2	399.3	273.6	255.3
146	519.6	240.2	233.1	467.7	254.3	397.7	273.8	255.3
147	518.8	240.3	233.2	468.0	254.6	396.1	274.1	255.3
148	517.9	240.7	233.4	468.5	254.9	394.1	274.4	255.2
149	517.3	240.7	233.5	468.6	254.8	392.4	274.8	255.2
150	516.0	240.7	233.3	468.6	254.8	390.8	275.1	255.3
151	515.0	240.9	233.3	468.6	254.9	389.2	275.4	255.2
152	514.2	241.0	233.8	468.9	255.1	387.5	275.5	255.2
153	513.1	241.1	233.8	468.9	255.2	386.0	275.8	255.2
154	512.0	241.4	233.7	468.6	255.2	384.7	276.1	255.3
155	511.0	241.6	234.0	468.7	255.4	382.8	276.3	255.2
156	510.0	241.8	234.0	468.6	255.5	381.4	276.6	255.2
157	509.0	242.1	234.2	468.6	256.0	379.8	276.7	255.1
158	507.9	242.0	234.3	468.6	256.0	378.3	276.9	255.1
159	506.4	242.2	234.2	468.1	255.7	377.3	277.1	255.3
160	505.4	242.4	234.3	467.9	256.0	375.7	277.3	255.3
161	504.4	242.4	234.4	467.9	256.1	374.0	277.6	255.2
162	503.4	242.8	234.8	467.9	256.4	372.6	277.8	255.1
163	502.0	242.8	234.5	467.5	256.3	371.2	278.0	255.2
164	501.0	243.2	234.7	467.1	256.5	369.9	278.0	255.2
165	499.9	243.1	234.7	467.1	256.6	368.6	278.4	255.2
166	498.8	243.2	235.1	466.8	256.8	367.2	278.5	255.1
167	497.5	243.6	235.0	466.2	256.9	366.1	278.6	255.2
168	496.5	243.7	235.3	466.2	257.2	364.8	278.9	255.1
169	495.3	243.6	235.4	465.7	257.3	363.4	279.0	255.1
170	493.9	243.7	235.1	465.2	257.2	362.3	279.3	255.2
171	492.6	244.0	235.2	464.8	257.3	368.5	279.4	255.3
172	491.5	244.1	235.2	464.3	257.4	355.2	279.5	255.3
173	490.4	244.3	235.3	463.9	257.5	340.6	279.9	255.3
174	489.5	244.6	235.8	463.6	257.8	326.0	280.0	255.1
175	488.3	244.7	236.0	463.2	257.9	312.4	280.1	255.2
176	486.8	245.2	236.0	462.6	257.9	300.0	280.3	255.2
177	485.8	245.2	236.0	462.1	258.0	287.6	280.5	255.3
178	484.9	245.2	236.5	462.0	258.2	275.3	280.8	255.2
179	483.5	245.5	236.2	461.3	258.1	266.9	280.9	255.3
180	482.3	245.8	236.5	460.7	258.3	261.7	281.0	255.3
181	481.0	245.9	236.6	460.2	258.4	256.0	281.2	255.2
182	479.9	245.8	236.5	459.6	258.6	252.4	281.5	255.3
183	478.9	246.2	236.7	459.2	258.8	249.3	281.6	255.3
184	478.1	246.1	236.9	459.0	259.0	247.9	282.0	255.2
185	476.6	246.1	236.6	458.1	258.9	245.6	282.2	255.3
186	475.5	246.2	236.7	457.7	259.0	244.3	282.4	255.3

[a]To correct TC2–TC6 for pegging of PRT2, subtract 18 ± 2 K from the tabulated data.
[b]PRT1 may be pegged at 231.2 K at entry. The entry temperature is estimated at 231.2 ± 1 K.

$241.5 - (18 \pm 2) = 223.5 \pm 1$ K, agrees with the STV range. Near the middle of the forebody frustum, the STV temperature was about 200 K and reasonably steady. The corrected initial temperature for TC4, about $218.6 - (18 \pm 2) = 200.6 \pm 2$ K, again agrees with the STV range. Near the nose, the STV temperature was about 193 K but rising about 0.5 K/h at the end of the test. The corrected initial temperatures for TC2 and TC3 data are about 197.5 ± 2 K, which are, as expected, slightly higher than the value that was measured at the end of the STV test.

Computational Models

This section describes the computational fluid dynamics (CFD) models, the material thermal response models, and the code coupling procedures used in this work.

CFD Models

The GIANTS code is used in this work to obtain flowfield solutions. GIANTS is an axisymmetric, nonequilibrium full Navier–Stokes equation solver that has been extensively modified to include unequal multicomponent diffusion, catalytic and ablating surface boundary conditions, an algebraic turbulence model, and procedures for coupling with material response solvers.[4,15] The chemistry model and other transport models are unchanged from those reported in Refs. 4 and 15.

Multicomponent diffusion is treated using a bifurcation approximation[16]:

$$D_{ij} = \bar{D}/F_i F_j \tag{1}$$

where $\bar{D}(T, P)$ is a reference diffusion coefficient and F_i is a diffusion factor for species i. The diffusion factors are considered to be constants because they are independent of pressure and relatively insensitive to changes in temperature. With this approximation and a few minor assumptions, the diffusive mass flux of species i in the surface-normal direction can be written as

$$j_i = -\frac{\rho \bar{D} \mu_2}{M \mu_1} \frac{\partial Z_i}{\partial \eta} \tag{2}$$

where the coefficients Z_i, μ_1, and μ_2 are defined as

$$Z_i = \frac{M_i x_i}{F_i \mu_2}, \qquad \mu_1 = \sum_i x_i F_i, \qquad \mu_2 = \sum_i \frac{M_i x_i}{F_i}$$

The bifurcation method properly conserves mass at every point in the flowfield and provides reasonable accuracy at relatively low computational cost when compared with exact solutions of the Stefan–Boltzmann equations for multispecies diffusion.[16] Suitable diffusion factors have been determined for most species in gas mixtures containing the elements H–C–N–O. The correlation $F_i \propto (M_i)^{0.489}$ is used as a default for computing F values that are not user specified.[16]

Unblown flowfield solutions at several trajectory points were computed using both the old diffusion model[17] and the bifurcation model. The bifurcation model, in general, predicts slightly higher surface heat flux for the Pathfinder entry. For example, Fig. 2 compares results at the peak laminar heating point in the Pathfinder trajectory. The bifurcation model results are about 10% above the results obtained using the old model.

In the Martian hypersonic entry environment, CO_2 dissociation produces significant quantities of CO and O that can recombine via surface-catalyzed reactions to form CO_2 and O_2. By the Rideal–Eley mechanism, this recombination proceeds by a sequence of first-order reactions involving a gas-phase species and surface-adsorbed species or available site:

$$\mathrm{O} + [_s] \rightarrow \mathrm{O}_s, \qquad \omega_1 = \gamma_1 c_{\mathrm{O}} \sqrt{\frac{RT_w}{2\pi M_{\mathrm{O}}}} \tag{3a}$$

$$\mathrm{CO} + \mathrm{O}_s \rightarrow \mathrm{CO}_2 + [_s], \qquad \omega_2 = \gamma_2 c_{\mathrm{CO}} \sqrt{\frac{RT_w}{2\pi M_{\mathrm{CO}}}} \tag{3b}$$

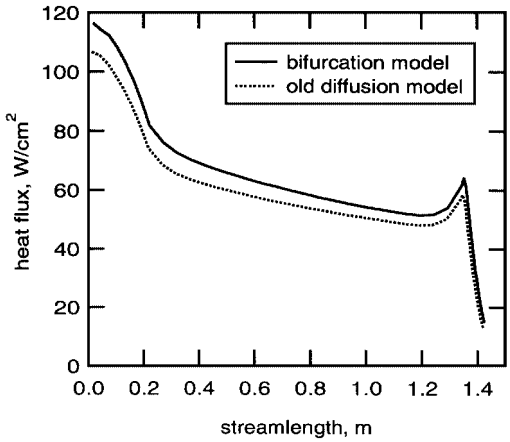

Fig. 2 Heat flux at 66 s predicted by GIANTS using bifurcation diffusion model and earlier diffusion model.

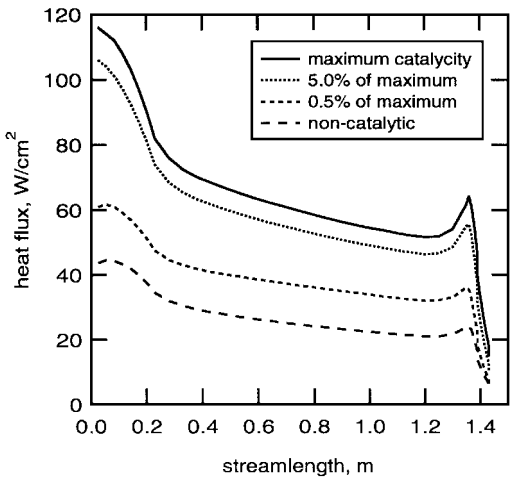

Fig. 3 Heat flux at 66 s predicted by GIANTS using varying degrees of surface catalycity.

$$\mathrm{CO} + [_s] \rightarrow \mathrm{CO}_s, \qquad \omega_3 = \gamma_3 c_{\mathrm{CO}} \sqrt{\frac{RT_w}{2\pi M_{\mathrm{CO}}}} \tag{3c}$$

$$\mathrm{O} + \mathrm{CO}_s \rightarrow \mathrm{CO}_2 + [_s], \qquad \omega_4 = \gamma_4 c_{\mathrm{O}} \sqrt{\frac{RT_w}{2\pi M_{\mathrm{O}}}} \tag{3d}$$

$$\mathrm{O} + \mathrm{O}_s \rightarrow \mathrm{O}_2, \qquad \omega_5 = \gamma_5 c_{\mathrm{O}} \sqrt{\frac{RT_w}{2\pi M_{\mathrm{O}}}} \tag{3e}$$

Although the catalycity of SLA-561V for these competing reactions has not been determined, the maximum recombination rate consistent with diffusion of CO and O to the wall can be calculated. This procedure sets $\gamma_5 = 0$ and either $\gamma_1 + \gamma_4 = 1$ or $\gamma_2 + \gamma_3 = 1$ depending on the ratio of c_{O} to c_{CO} at the wall.[5,9] By setting one of the sums equal to unity, the model assumes every surface collision by either O or CO is effective in advancing one of the reaction steps in Eqs. (3a–3d). A partially catalytic surface is approximated by using a fraction of the maximum rate; however, this procedure neglects O_2 formation that can occur via nonzero γ_5 in Eq. (3e). A general algorithm for GIANTS that allows partial catalycity for both CO_2 and O_2 formation has not yet been developed. Therefore, the fully catalytic model is used for most GIANTS results presented in this work.

Figure 3 compares results at the peak heating trajectory point using the bifurcation diffusion model and varying efficiency for surface recombination. Assuming 5.0 and 0.5% recombination results in about 10 and 40% lower heating, respectively, compared with the fully catalytic case. This heating reduction is exaggerated, however, because the model does not account for heat released by O_2 formation by Eq. (3e). Although a rigorous quantitative analysis

of a partially catalytic surface was not possible, these results suggests that, if the peak catalycity of SLA-561V is on the order of 1%, a reduction in peak heating of about 15% from the fully catalytic value may be expected.

Flowfield turbulence is treated using the Baldwin–Lomax algebraic model[18] implemented in the same manner as described in Ref. 19. In the inner region, the turbulent viscosity is calculated from the Prandtl–Van Driest formulation:

$$(\mu_t)_i = \rho(\eta\kappa D)^2|\varpi| \tag{4}$$

The Van Driest damping in Eq. (4) is given by

$$D = 1 - \exp\left[-(y^+/26)(\rho/\rho_w)^{\frac{1}{2}}(\mu_w/\mu)\right] \tag{5}$$

in which the effects of compressible and nonisothermal flow are included. In the outer region, the turbulent viscosity is calculated from

$$(\mu_t)_O = 0.0168\rho C_{cp} F_{\text{wake}} F_{\text{kleb}} \tag{6}$$

where F_{kleb} is the Klebnoff intermittence factor,[20] $C_{cp} = 1.6$, and

$$F_{\text{wake}} = \min[\eta_{\max} F_{\max}, \eta_{\max} V_{\text{dif}}/F_{\max}] \tag{7}$$

V_{dif} is the difference in the maximum and minimum velocity magnitudes in the profile, and the quantities $\eta_{\max}$ and $F_{\max}$ are determined from $F(\eta) = \eta|\varpi|D$ as the values at the first maximum of $F(\eta)$ away from the wall.

Material Response Models

The forebody heatshield ablator for Pathfinder is SLA-561V. This material is similar to that flown on the Viking Mars missions, the major differences being a higher bulk density because of a reduced honeycomb size and greater blowing rate and char shrinkage because of different processing of the ingredients in the ablative compound. Arcjet tests were conducted to characterize and qualify this material for the Pathfinder entry conditions.[21] Radiant heating tests were performed later.[22]

As a result of these tests, updated material property and ablation models were developed at Applied Research Associates (ARA), NASA Ames Research Center (ARC), and Lockheed Martin Astronautics (LMA).[2,4,6] The ARA model uses the CMA code,[23] the ARC model uses CMA or FIAT,[24] and the LMA model was developed for the REKAP code.[25] All three codes solve well-known equations for charring material ablation, but the numerical treatment of the pyrolysis and ablation models is not identical. For this work, ARA and LMA agreed to perform material response calculations for the nose and corner TC locations for the purpose of comparison with the data. For FIAT calculations performed at ARC, the heatshield material was subdivided into 50 computational cells, and rigorous time-step constraints were enforced to maintain the time accuracy of the solutions.

The vertical backplate and part of the backshell were covered with SIRCA tiles. A nonablating, charring model for this material was developed and validated against arcjet data.[26] FIAT solutions using this material model match the nonablating surface and in-depth temperature response of SIRCA for hot-wall heat fluxes up to about 50 W/cm^2.

Code Coupling Procedures

Several options are available for coupling GIANTS with material response solvers. The degree of coupling required in any given problem depends primarily on the magnitude of the surface blowing rate relative to the freestream mass flux. For problems with relatively low blowing, it is usually adequate to solve the flow equations only once at each selected trajectory point using radiative equilibrium wall temperature boundary conditions.[26,27]

For the general case of fully coupled blown solutions, general surface mass and energy balances for GIANTS can be written as[28]

$$\dot{m}_g y_{gi} + \dot{m}_c y_{ci} - (\rho v)_w y_{wi} - j_i = M_i \sum_r \omega_{ri} \tag{8}$$

$$q_w + \alpha_w q_{\text{rad}} - (\rho v)_w h_w = \sigma\varepsilon_w T_w^4 + q_{\text{cond}} - \dot{m}_c h_c - \dot{m}_g h_g \tag{9}$$

where the surface blowing rate is

$$(\rho v)_w = \dot{m}_g + \dot{m}_c \tag{10}$$

and the aerothermal heat flux is

$$q_w = \left[k_T \frac{\partial T_T}{\partial \eta} + k_V \frac{\partial T_V}{\partial \eta} - \sum_i j_i h_i\right]_w \tag{11a}$$

At the stagnation point, the radiative heat flux can be estimated from correlations.[29]

The material response solution only needs the surface energy balance, Eq. (9), as a boundary condition, but the aerothermal heating is usually written in convective heat transfer form as

$$q_w = C_H(H_R - h_w) \tag{11b}$$

Thus, to couple the fluid and solid solutions, procedures have been developed for calculating appropriate values of H_R and C_H at each surface node of the GIANTS solution.[4]

For any trajectory point, the first solution is obtained by GIANTS using the unblown, radiative equilibrium wall temperature boundary conditions

$$-j_i = M_i \sum_r \omega_{ri}, \qquad q_{w,\text{RE}} = \sigma\varepsilon_w T_{w,\text{RE}}^4 \tag{12}$$

in lieu of Eqs. (8) and (9). The unblown hot-wall heat transfer coefficient is

$$q_{w,\text{RE}} = C_{H1}(H_R - h_{w,\text{RE}}) \tag{13}$$

and the material response is calculated using the blowing correction

$$\frac{C_H}{C_{H1}} = \frac{2\lambda B_1'}{\exp(2\lambda B_1') - 1}, \qquad B_1' = \frac{(\dot{m}_c + \dot{m}_g)}{C_{H1}} \tag{14}$$

The quantities C_{H1}, H_R, λ, and P are time-dependent input parameters for the material response solvers that determine the blowing rates, the surface temperature, and the conduction heat flux as a function of time and location. The heat of ablation (mostly carbon oxidation for Pathfinder) enters into the material response calculation through the h_w term that appears in Eqs. (9) and (11b).

If the blowing rate is not too large, for laminar flow the classical value $\lambda = 0.5$ is a good approximation, whereas for turbulent flow a smaller value, such as $\lambda = 0.35$, is more appropriate.[23] This approach is especially convenient for comparing solutions of different material models because it is computationally expensive to perform repeated coupled blown solutions following Eqs. (8–11).

If necessary, GIANTS can determine a quasisteady solution consistent with surface-location dependent values of $\dot{m}_g$, T_w, and q_{cond} determined by a material response code. The blown transfer coefficient C_H is then computed by Eq. (11b) and used by the material response solver in Eq. (9). Depending on the complexity of the problem, several iterations between the two codes may be required to ensure both solutions use the same values for q_w. Both codes require material property data, such as surface and bulk properties and species concentrations of ablation and pyrolysis products.

This iterative coupled procedure was employed by Chen et al.[4] Unfortunately, the blown and unblown flowfield solutions were not saved, and so the solutions cannot rigorously be checked to determine whether or not the iterative coupling was actually necessary for the TPS response and sizing analysis. Based on the tabulated and plotted results from that work, the stagnation point H_R and C_{H1} histories were estimated, and the material response was recalculated using the blowing parameter $\lambda = 0.5$. Figure 4 compares the surface temperature history obtained using the iteratively coupled and blowing correction techniques. The agreement is very good considering there was some uncertainty in extracting the unblown parameters, particularly for the lower pressure solutions at early times.

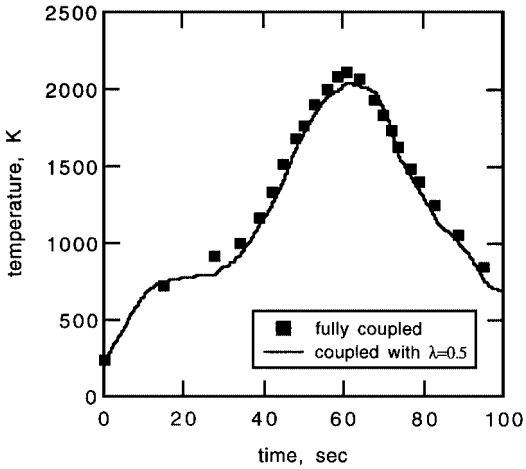

Fig. 4 Stagnation-pointsurface temperature history obtained by FIAT using iterative coupled procedure or blowing reduction parameter.

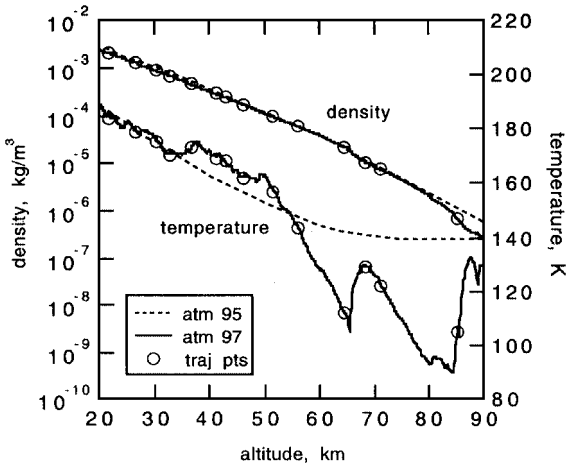

Fig. 5 Preflight and reconstructed atmospheric structures; circles indicate GIANTS trajectory points.

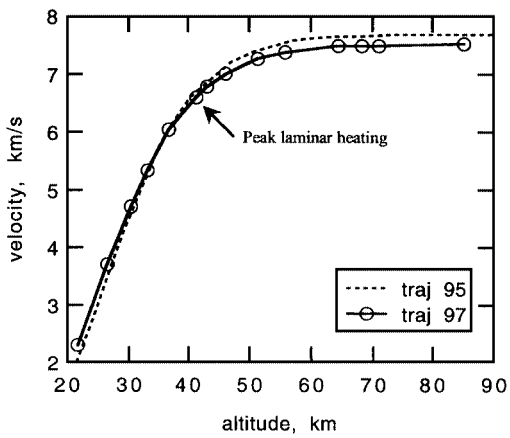

Fig. 6 Preflight shallow and reconstructed Pathfinder entry trajectories; circles indicate GIANTS trajectory points.

Aerothermal Heating Results

The Martian atmospheric structure and the Pathfinder entry trajectory up to 133.3-km altitude were reconstructed using data from accelerometers and other atmosphere structure sensors.[7,30] The atmosphere and trajectory between 20- and 90-km altitude are shown in Figs. 5 and 6, respectively. The circles indicate 14 trajectory points, listed in Table 4, that were selected to define the nosetip peak heating point and the general shape of the forebody heating profile. Also shown in Figs. 5 and 6 are the atmosphere and the shallow design trajectory used by Chen et al.[4]

Table 4 Trajectory points for GIANTS calculations

Time, s	Velocity, m/s	Altitude, km	Temperature, K	Density, kg/m^3
30	7504	85.000	105	6.74E−07
40	7496	71.109	122	7.24E−06
42	7490	68.469	129	1.01E−05
45	7472	64.599	112	2.10E−05
52	7364	56.026	143	5.76E−05
56	7242	51.445	157	9.28E−05
61	6994	46.089	162	1.69E−04
64	6774	43.097	168	2.31E−04
66[a]	6596	41.204	169	2.80E−04
71	6041	36.854	173	4.38E−04
76	5333	33.082	170	6.68E−04
80	4717	30.489	175	8.53E−04
87	3704	26.760	179	1.24E−03
100	2299	21.848	184	2.01E−03

[a]Peak laminar stagnation-point heating.

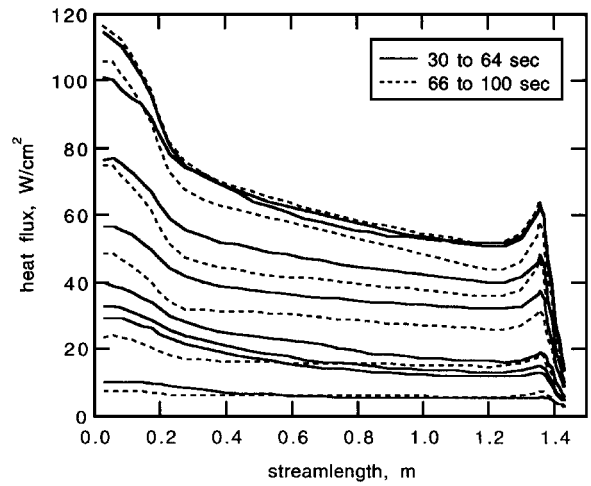

Fig. 7 Laminar heating profiles.

The new reconstructedatmospheric density profile is almost identical to the old model. The reconstructed atmospheric temperature profile is irregular but stays within 10 K of the older model except at the highest altitudes, where deviations up to 50 K are seen. These temperature differences are not significant for CFD heating analyses because the freestream energy is mostly kinetic at high altitude. The actual entry was steeper than the design trajectory, and peak heating occurs at almost identical velocity but 500-m higher altitude.

Using the reconstructed trajectory and atmospheric structure, the aerothermal heating environment was computed using the modified version of the GIANTS code and numerical procedures described earlier. The calculations were performed using the Cray C-90 supercomputer at ARC, a 42 × 62 grid, and assuming radiative equilibrium surface temperature for an unblown fully catalytic wall. A grid sensitivity study was performed to ensure that the grid was adequate for both laminar and turbulent flow calculations. For laminar cases the grid was almost identical to the grid used in Ref. 4.

From base pressure measurements on the Mars Vikings probes,[31] it was inferred that turbulence first occurred at $Re_\infty = 6\text{–}9 \times 10^5$. For Mars Pathfinder this range of Reynolds numbers occurred at 67.0–73.5 s, which is 1–7.5 s after peak stagnation-point heating. Therefore, both laminar and turbulent flow solutions were obtained for the last six trajectory times starting at 66 s. The flow was assumed to be fully turbulent starting at the first cell off the nose.

Laminar heat flux distributions for different times are presented in Fig. 7. These results are typical in the sense that the heat flux is highest at the stagnation point and decreases with increasing streamlength up to the shoulder. As the flow accelerates around the shoulder, there is an increase in heat flux followed by a sharp decrease. The stagnation-point heating reaches a maximum of 116 W/cm^2 at 66 s.

Turbulent heat flux distributions for different times are shown in Fig. 8. There is a small increase in heat flux on the spherical nose (118 W/cm^2) compared with the laminar flow solutions. The

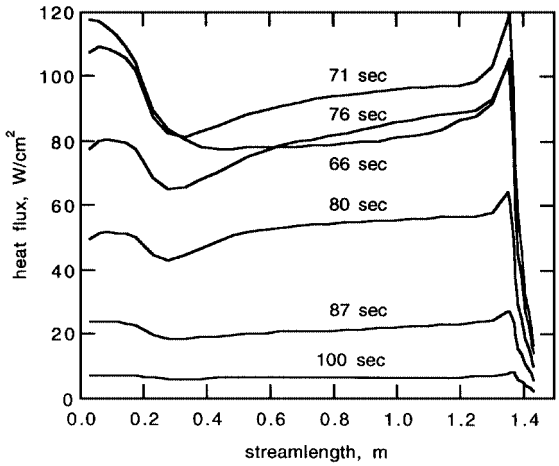

Fig. 8 Turbulent heating profiles.

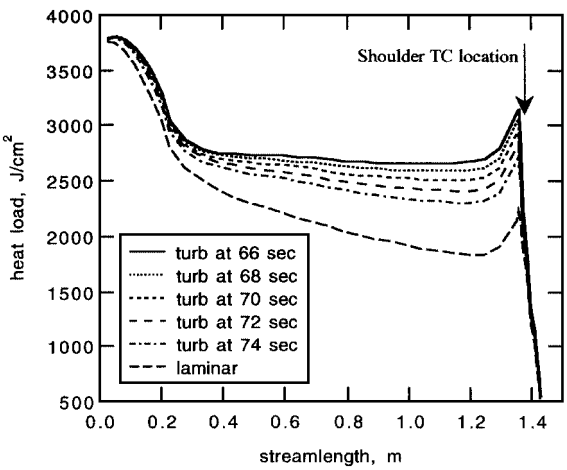

Fig. 9 Heat load profiles.

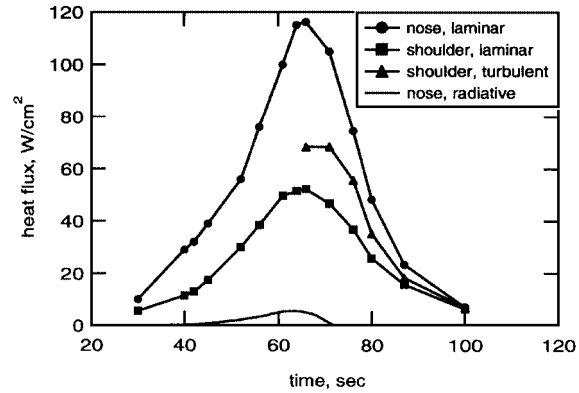

Fig. 10 Heating histories at stagnation point and shoulder TC locations.

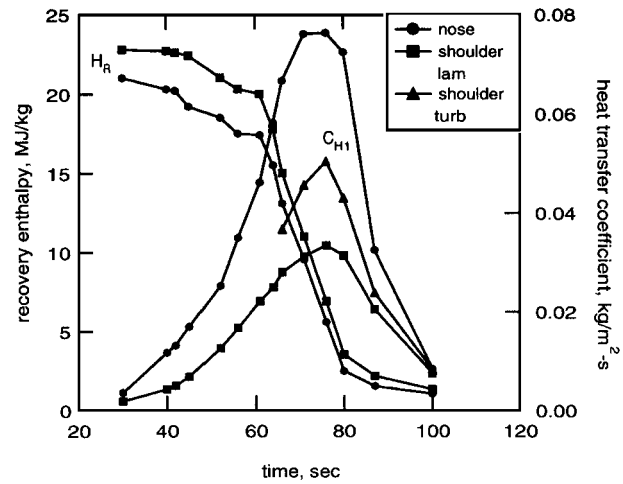

Fig. 11 Convective boundary conditions at stagnation point and shoulder TC locations.

turbulent heat flux has a local minimum after the sphere–cone junction ($S = 0.28$–0.38) then increases along the length of the frustum. The predicted peak shoulder heating exceeds the stagnation-point value at all times except 66 s. For this first case, $Re_\infty = 5.5 \times 10^5$ is probably too low for the flow to be turbulent. The maximum heat flux of 120 W/cm^2 occurs on the shoulder for turbulent flow at 71 s. The calculations do not exhibit the very large increase in heating at the start of the frustum seen in Ref. 8.

Laminar and turbulent heat load distributions are presented in Fig. 9. Five turbulent cases are shown corresponding to onset of turbulence at different times between 66 and 74 s. The peak heat load on the nose is about 3.8 kJ/cm^2. In all cases the heat load decreases along the length of the frustum up to the shoulder. On the shoulder the heat load increases 0.5–0.7 kJ/cm^2 but stays below the value seen on the spherical nose. After the local maximum on the shoulder, the heat load decreases to about 0.5 kJ/cm^2 at the end of the computational grid.

Figure 10 shows the heating history at the stagnation point and at the shoulder TC location. As mentioned earlier, the peak heat flux and heat load at the stagnation point are 118 W/cm^2 and 3.8 kJ/cm^2, respectively. Also shown is the stagnation-point radiative heat flux estimated by correlation.[29] The peak radiative heat flux and heat load are 5.53 W/cm^2 and 88.7 J/cm^2. These values are less than 5% of the peak convective heating and 2.5% of the convective heat load, respectively. At the shoulder TC location, both laminar and turbulent heat flux are shown. Depending on the onset time for turbulence, the peak heat flux is 52.6–68.5 W/cm^2, and the heat load is 1.84–2.16 kJ/cm^2. These values are low because the shoulder TCs were located in the region where the heat flux and load decrease very rapidly, i.e., about 2 cm past the local maximum in Figs. 7–9. Within ±2 cm of this TC location, the predicted heat load varies from 1.27 to 2.21 kJ/cm^2 for laminar flow and from 1.33 to 3.14 kJ/cm^2 for the turbulent flow cases. It will be difficult if not impossible to draw firm conclusions about the flowfield turbulence because of the poor positioning of the shoulder TCs.

Finally, for purposes of conducting a thermal analysis of the heatshield, the results from Fig. 10 were converted into equivalent convective boundary condition parameters C_{H1} and H_R presented in Fig. 11. The peak heat transfer coefficient is estimated at 0.076 kg/m^2-s at the nose and 0.033–0.050 kg/cm^2-s on the shoulder. These values were obtained for a fully catalytic surface. However, based on results of several cases run with partial catalycity at different trajectory times (cf. Fig. 3), an overall reduction of about 15% in heat transfer coefficient may be appropriate for modeling a realistic material.

Forebody Thermal Analysis

Most of the inside surface of the spacecraft structure was covered by a multilayer blanket insulation. Because of the presence of this insulation and the effectiveness of the internal heat rejection system,[14] heat conduction from the interior of the spacecraft to space was low. Thus, although the temperature of the heatshield depended on orientation to the sun, the temperature gradient across the SLA-561 thickness was negligible (about 1 K) because of the presence of the insulation. This small gradient is confirmed by the initial entry temperatures (TCs 2 and 3 and TCs 5 and 6) and the STV test data.[14]

Convective heating conditions from Fig. 11 were input as boundary conditions to the material response models. The heat transfer coefficient was extrapolated to zero at 20 and at 101 s. The convection was ended abruptly because it is difficult to reliably model convective cooling, which may occur late in the trajectory as the freestream velocity and enthalpy decrease. After 101 s, the surface was allowed to cool only by reradiation to an environment at an effective temperature of 200 K. Stagnation-point convective heating

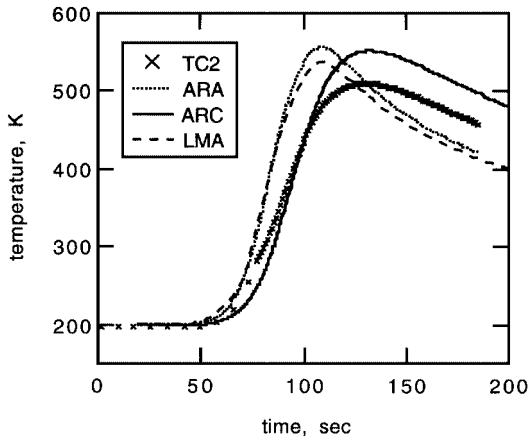

a) 100% of laminar heating

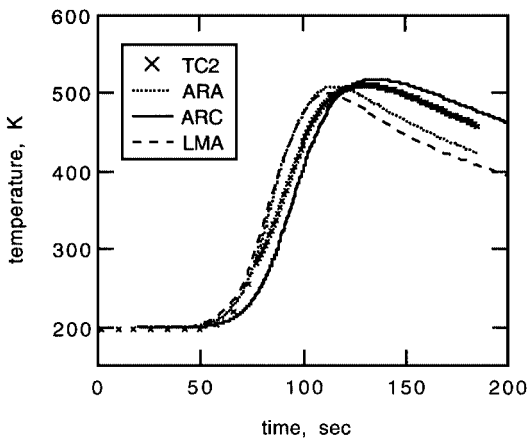

b) 85% of laminar heating

Fig. 12 Corrected data and predictions for temperature history at location of stagnation-point midthickness TC.

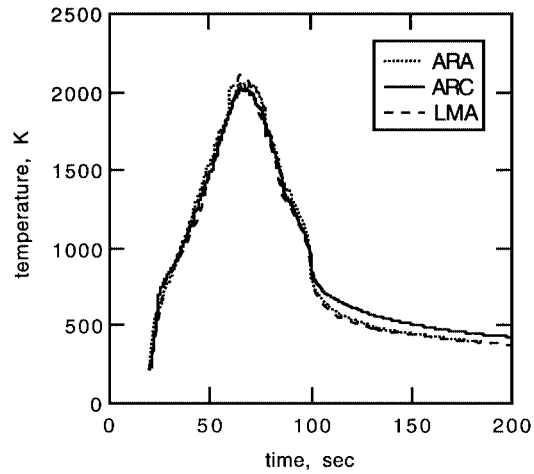

Fig. 13 Surface temperature predictions for scaled (85%) stagnation-point heating.

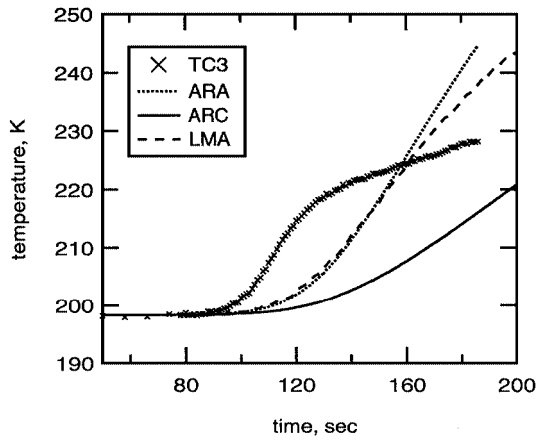

Fig. 14 Corrected data and predictions for temperature history at location of stagnation-point bondline TC.

was augmented with the radiative heating profile from Fig. 10. Radiation was assumed to be negligible at the shoulder.

Material response calculations were performed at ARA, ARC, and LMA using different material property models and thermal response codes. Results using unscaled (100%) and scaled (85%) GIANTS stagnation-point heating are presented in Figs. 12a and 12b, respectively. For Fig. 12b, the heat transfer coefficient was scaled, but the recovery enthalpy was unchanged. The corrected TC2 data are the symbols. Each material model exhibits different behavior, but some trends are apparent. Using 100% heating all three models overpredict the data by 26–46 K, but with 85% scaling the models provide a better approximation to the data. For both cases, the LMA model gives the lowest peak temperature, and the ARA model gives the highest peak temperature at the earliest time. From 150 to 200 s, the temperature decay rates roughly match the slope of the data, but the values are off by up to 50 K. The ARC model provides the best match to the data, but the initial temperature rise is too slow.

Surface temperature histories obtained from the three codes for scaled (85%) stagnation-point heating are shown in Fig. 13. The ARC and LMA models predict the lowest and highest peak temperatures, 2021 and 2106 K, respectively. The three ablation models are quite different. The predicted recession varied from 0.00 cm for the ARC model to 0.34 cm for the ARA model. The peak blowing rates show less variation, from 0.020 to 0.031 kg/m^2-s with the ARC and ARA models predicting the lowest and highest blowing rates, respectively. At the peak blowing rate of the ARA model, the surface mass flux is less than 2% of the freestream mass flux. After 100 s, the low-ablation ARC model cools down least rapidly because this model retains more mass and thermal energy within the material.

The disparity in surface recession predictions is a consequence of differences in the ablation models. The ARC model assumes formation of a silica surface with negligible recession rate for unblown, hot-wall heat flux up to 120 W/cm^2. The ARA and LMA models are calibrated to match measured recession in relatively long-duration tests at a few heating rates (at least 30-s exposure up to 143 W/cm^2). Arcjet testing in air shows that below about 90 W/cm^2, SLA-561V forms a black char with low recession rate. From 90 to 120 W/cm^2, a coherent melt layer forms by coalescence of silica microballoons and fibers.[6] In this melt-formation regime, although the surface recedes, the mass loss is not proportional to the apparent recession because the coalescence phenomenon densifies the surface. Nevertheless, some surface mass loss occurs because of carbon oxidation and possible spall of melt or solid particles induced by pyrolysis gas blowing. Thus, the silica-surface model underestimates the surface mass loss, whereas the models that match apparent surface recession overestimate the surface mass loss. For the scaled Pathfinder stagnation-point heating, the peak hot-wall heat flux is above 90 W/cm^2 for less than 10 s and the peak heat flux is only 103 W/cm^2. For such short-duration exposure to the melt-formation regime, the recession should be below correlated steady-state predictions and closer to the ARC prediction. This observation may explain why the ARC model provides a better match to the data in Fig. 12b (see also subsequent figures).

Bondline temperature predictions are compared with corrected TC3 data in Fig. 14. No calculation matches the abrupt rise and subsequent slope change of the data. The fast initial rise can be approximated by reducing the thermal conductivity of the structure, but the slope change does not occur until much later. Note, however, that unusual bondline temperature response has been observed previously for this material in both arcjet and thermal flash tests. The unusual behavior, which has been attributed to direct transmission of thermal radiation to the bondline, is manifest as a blip of energy appearing too early in the TC measurements.[22]

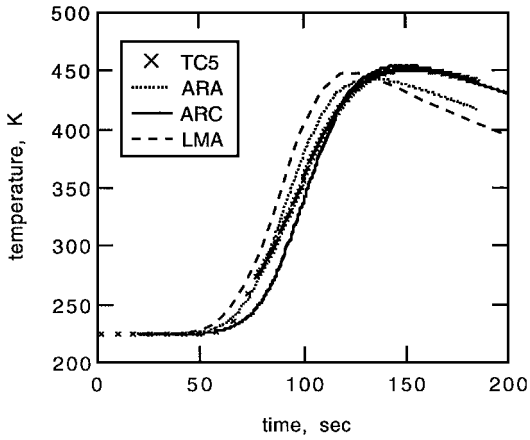

a) Laminar heating

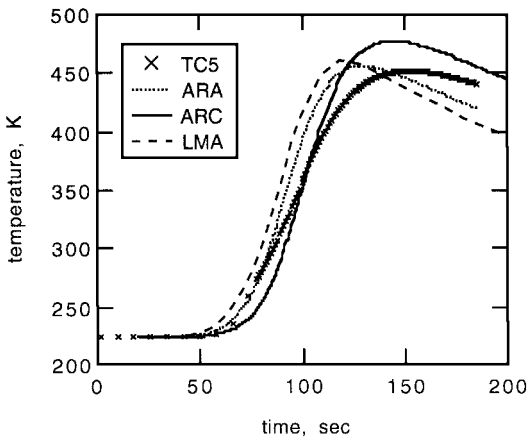

b) Turbulent heating after 66 s

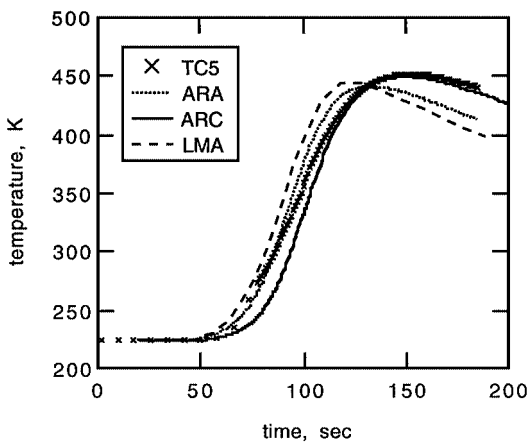

c) 85% of turbulent heating

Fig. 15 Corrected data and predictions for temperature history at location of shoulder midthickness TC.

For the shoulder thermocouple location, material response was calculated using GIANTS laminar heating, turbulent heating with early transition at 66 s, and scaled (85%) turbulent heating with the same early transition. Results from the three cases are presented in Figs. 15a–15c. The corrected TC5 data are the symbols. For the fully turbulent case, all three models overpredict the maximum temperature. The laminar and scaled turbulent cases provide a better match to magnitude and timing of the maximum temperature. The scaled turbulent cases are slightly below the laminar flow cases. Because of the poor location of the shoulder TCs, the disagreements between the material models, and the uncertainty of CFD predictions for Mars entries (perhaps ±15% in heating), it is impossible to determine when turbulence occurs or the degree of surface catalycity based on these data.

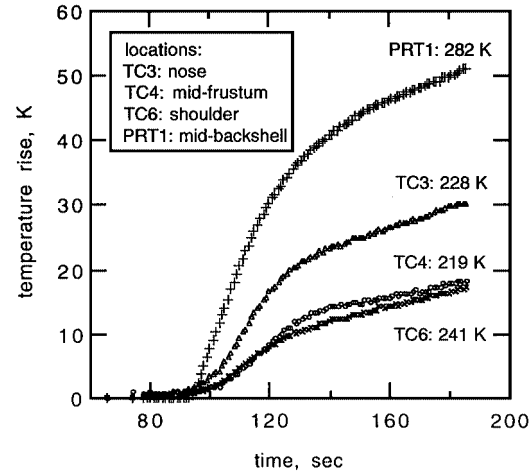

Fig. 16 Bondline temperature rise at four locations.

For the three cases, the peak hot-wall heat flux ranges from 52.8 to 68.5 W/cm^2 and is significantly lower than the stagnation-point value (see Fig. 10). Based on arcjet test data and the short duration of the heat pulse, surface recession at the shoulder TC location should be negligible. The predicted recession varied from 0.00 cm for the ARC model to between 0.13 and 0.17 cm for the LMA and ARA models. As discussed earlier, the actual recession probably is between these predictions, but closer to the ARC model.

Figure 16 compares the temperature rise measured by the bondline sensors TC3, TC4, TC6, and PRT1. Figure 16 also gives the maximum final temperature measured by each device. All bondline temperature stayed well below the design limit of 520 K, which shows there was sufficient heatshield thickness margin for the actual entry. The bondline TC data are not very useful for quantitative analysis of surface aerothermal heating because the depth is too great and the heatshield material exhibits unusual energy transmission to the bondline (cf. Fig. 14). Qualitatively, the TC data suggest the mid-frustum and shoulder locations experienced comparable heating that was significantly below the level experienced at the stagnation point.

The backshell thermocouple, which was beneath a relatively thin layer of SLA-561S, measured a substantial thermal response that may be amenable to analysis. LMA has a material model for this material, but did not provide any thermal analysis for this paper.

Aft Heating and Material Response

Three TCs were located near the surface of the SIRCA tiles at the rear of the Pathfinder vehicle. Thermocouples TC7 and TC8, which were on the vertical backplate, failed prior to entry and returned no useful data. Thermocouple TC9, which was on the backshell frustum about 6 cm forward of the vertical backplate, appeared to function normally. The aft isothermal block temperature, as measured by PRT3, remained near 255.6 K throughout entry. This value was within the calibration range of the sensor; therefore, the TC9 data in Table 3 require no correction.

On approach to Mars, the SIRCA tiles were not insulated; nevertheless, the outer surface was relatively warm because during cruise the backplate faced the solar panel array and the cruise-stage shunt radiator, which were warmer than surrounding space. The temperature at cruise-stage separation (−900 s) was measured at 245 K by TC9. After cruise-stage separation, the backplate was exposed to space with the sun about 41 deg off the aft centerline, and TC9 showed a gradual temperature decrease to 233 K in 900 s. This temperature decrease can be approximated by assuming radiation to space at a temperature of 200 K after cruise-stage separation. The resulting nonuniform temperature distribution provides an initial condition for the entry thermal analysis.

It was beyond the scope of this work to perform afterbody CFD simulations, which are computationally expensive and not necessarily reliable. Instead, the material response was calculated using prescribed surface heating profiles, and the surface was allowed to cool by radiation only. Internal heat conduction and pyrolysis were calculated using the standard FIAT material model for SIRCA.[26]

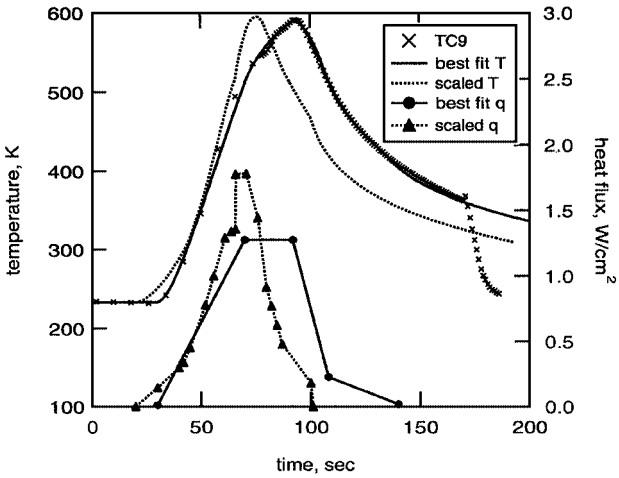

Fig. 17 Heat flux profiles, temperature data, and predictions for aft near-surface TC.

Two heat flux profiles were used. The first was the turbulent corner heating scaled by a factor of 0.026, and the second was a simple profile created to fit the data. The TC9 data and FIAT predictions are presented in Fig. 17. The TC9 temperature increased to a maximum of 591 K at 93 s and then cooled gradually until parachute deployment at 171 s significantly changed the convective environment. The forebody TCs did not note the parachute deployment because of their greater depths within the heatshield. The measured peak temperature can be matched by using 2.6% scaling of the turbulent corner heating, but the shape of TC response is incorrect. The scaled profile is too narrow. A very good match is obtained with the simple five-point profile shown at the bottom of Fig. 17. This profile has low heat load and peak heat flux of 70 J/cm^2 and 1.28 W/cm^2, respectively. This estimated peak heating is below the values of about 2.5 and 1.6 W/cm^2 calculated for this afterbody location on Pathfinder.[9,10] The long-duration afterbody heat pulse is consistent with results reported by Olynick et al.[11] for the Stardust vehicle.

The surface temperature of SIRCA must exceed about 800 K for a dark-colored char to form. Certainly this temperature was not reached at the location of TC9, which recorded a maximum temperature under 600 K. The white-colored appearance of the aft cover in photographs taken by the Sojourner rover supports this observation.

Conclusions

The Mars Pathfinder probe contained instrumentation to measure heatshield temperatures during entry. A description of the experiment, the entry data, and required corrections to the data were presented. Three TCs failed, but useful data were obtained from six others including a midthickness TC at the stagnation point, a midthickness TC on the shoulder, and a near-surface TC at the aft end of the backshell.

The aerothermal environment on the forebody was calculated using the GIANTS code with a bifurcation diffusion model and a Baldwin–Lomax turbulence model. The calculations showed a peak unblown radiative-equilibrium heat flux of 118 W/cm^2 at the stagnation point and 120 W/cm^2 on the shoulder for turbulent flow. The heat load was 3.8 kJ/cm^2 on the nose, decreasing along the frustum, then increasing to 2.7–3.1 kJ/cm^2 on the shoulder depending on the onset time for turbulence.

One-dimensional charring material response was calculated using three different models. Stagnation-point temperature data were consistent with about 85% of fully catalytic laminar heating. Shoulder temperature data were consistent with fully catalytic laminar heating or with about 85% of fully catalytic heating with early onset of turbulence. The bondline temperature data were not amenable for quantitative analysis of the aerothermal heating but clearly showed the heatshield had sufficient thickness margins for the actual entry. The aft TC data indicated the peak heat flux and heat load were about 1.3 W/cm^2 and 70 J/cm^2, respectively. The aft heating profile was about 20 s longer than the forebody heating profile.

Acknowledgments

This work would not have been possible without the assistance of numerous people at the Jet Propulsion Laboratory, Lockheed Martin Astronautics, and NASA Ames Research Center. In particular, the authors acknowledge the efforts of H. K. Tran for the thermocouple plug design, D. C. Gruel for the temperature data reconstruction, K. S. Novak for the solar thermal vacuum and in-flight vehicle health check data, and C. T. Edquist for REKAP analyses.

References

[1]"Aeroshell—ICD," Jet Propulsion Lab., Drawing 10158741, rev. B, California Inst. of Technology, Pasadena, CA, July 1995.

[2]Congdon, W. M., Edquist, C. T., and Henline, W. D., "Thermal Protection Studies for the 1996 Pathfinder Mission to Mars," AIAA Paper 94-0249, Jan. 1994.

[3]"Thermal Protection System Installation, Backshell Interface Plate," Jet Propulsion Lab., Drawing 10158708, rev. A, California Inst. of Technology, Pasadena, CA, April 1996.

[4]Chen, Y.-K., Henline, W. D., and Tauber, M. E., "Mars Pathfinder Trajectory-Based Heating and Ablation Calculations," *Journal of Spacecraft and Rockets*, Vol. 32, No. 2, 1995, pp. 225–230.

[5]Gupta, R. N., Lee, K. P., and Scott, C. D., "Aerothermal Study of Mars Pathfinder Aeroshell," *Journal of Spacecraft and Rockets*, Vol. 33, No. 1, 1996, pp. 61–69.

[6]Congdon, W. M., "Ablation Model Validation and Analytical Sensitivity Study for the Mars Pathfinder Heat Shield," AIAA Paper 95-1888, June 1996.

[7]Spencer, D. A., Blanchard, R. C., Braun, R. D., Kallemeyn, P. H., and Thurman, S. W., "Mars Pathfinder Entry, Descent, and Landing Reconstruction," *Journal of Spacecraft and Rockets*, Vol. 36, No. 3, 1999, pp. 357–366.

[8]Mitcheltree, R. A., "Computational Aerothermodynamics for Mars Pathfinder Including Turbulence," AIAA Paper 95-3493, Aug. 1995.

[9]Mitcheltree, R. A., and Gnoffo, P. A., "Wake Flow About the Mars Pathfinder Entry Vehicle," *Journal of Spacecraft and Rockets*, Vol. 32, No. 5, 1995, pp. 771–776.

[10]Haas, B. L., and Venkatapathy, E., "Mars Pathfinder Computations Including Base-Heating Predictions," AIAA Paper 95-2086, June 1995.

[11]Olynick, D. R., Chen, Y.-K., and Tauber, M. E., "Wake Flow Calculations for the Stardust Sample Return Capsule," *Journal of Spacecraft and Rockets* (submitted for publication); also AIAA Paper 97-0277, Jan. 1997.

[12]Moss, J. N., Blanchard, R. C., Wilmoth, R. G., and Braun, R. D., "Mars Pathfinder Rarified Aerodynamics: Computations and Measurements," *Journal of Spacecraft and Rockets*, Vol. 36, No. 3, 1999, pp. 330–339.

[13]Schofield, T., "AIP Data Conversion Expressions—Revision B," Jet Propulsion Lab., Interoffice Memorandum DFM 96-014, California Inst. of Technology, Pasadena, CA, Dec. 1996.

[14]Lyra, J. C., and Novak, K. S., "The Mars Pathfinder System Level Thermal Vacuum Test," AIAA Paper 97-2454, June 1997.

[15]Olynick, D. R., and Henline, W. D., "Numerical Benchmarks for Navier–Stokes Heating Calculations on Access to Space Vehicles," AIAA Paper 95-2078, June 1995.

[16]Bartlett, E. P., Kendall, R. M., and Rindal, R. A., "An Analysis of the Coupled Chemically Reacting Boundary Layer and Charring Ablator. Part IV: A Unified Approximation for Mixture Transport Properties for Multicomponent Boundary-Layer Applications," NASA CR-1063, June 1968.

[17]Gnoffo, P. A., Gupta, R. N., and Shinn, J. L., "Conservation Equations and Physical Models for Hypersonic Air Flows in Thermal and Chemical Nonequilibrium," NASA TP-2867, Feb. 1989.

[18]Baldwin, B. S., and Lomax, H., "Thin Layer Approximation and Algebraic Model for Separated Turbulent Flows," AIAA Paper 78-0253, Jan. 1978.

[19]Chen, Y.-K., Henline, W. D., Olynick, D. R., and Palmer, G. E., "Three-Dimensional Hypersonic Flowfields and Heating Analysis over DC-3 Vehicle," AIAA Paper 95-2081, June 1995.

[20]Shirazi, S. A., and Truman, C. R., "Evaluation of Algebraic Turbulence Models for PNS Predictions of Supersonic Flow Past a Sphere–Cone," *AIAA Journal*, Vol. 27, No. 5, 1989, pp. 560–568.

[21]Tauber, M., Tran, F., Hui, F., Wercinski, P., Tran, D., Chen, Y., and Cartledge, A., "Mars/Pathfinder Heat Shield Design Verification Arc-Jet Tests," NASA Ames Research Center, March 1995.

[22]Congdon, W. M., "Thermal Radiation Characteristics of the Mars Heat Shield Material for Flight Data Analysis," AIAA Paper 96-2129, June 1996.

[23]Moyer, C. B., and Rindal, R. A., "An Analysis of the Coupled Chemically Reacting Boundary Layer and Charring Ablator, Part II, Finite Difference Solution for the In-Depth Response of Charring Materials Considering Surface Chemical and Energy Balances," NASA CR-1061, June 1968.

[24]Chen, Y.-K., and Milos, F. S., "Fully Implicit Ablation and Thermal Analysis Program (FIAT)," *ICCE/4, Fourth International Conference on Composites Engineering*, edited by D. Hui, International Community for

Composites Engineering and College of Engineering, Univ. of New Orleans, New Orleans, LA, 1997, pp. 661, 662.

[25]Gordon, P., "Analysis of One-Dimensional Heat Conduction Computer Program," Re-Entry Systems Operations, General Electric Co., Rept. GE-RSD TIS-R66S-D10, Philadelphia, PA, March 1966.

[26]Chen, Y.-K., and Milos, F. S., "Ablation and Thermal Response Program for Spacecraft Heatshield Analysis," *Journal of Spacecraft and Rockets*, Vol. 36, No. 3, 1999, pp. 475–483; also AIAA Paper 98-0273, Jan. 1998.

[27]Chen, Y.-K., and Milos, F. S., "Solution Strategy for Thermal Response of Nonablating Thermal Protection Systems at Hypersonic Speeds," AIAA Paper 97-0615, Jan. 1997.

[28]Milos, F. S., and Rasky, D. J., "Review of Numerical Procedures for Computational Surface Thermochemistry," *Journal of Thermophysics and Heat Transfer*, Vol. 8, No. 1, 1994, pp. 24–34.

[29]Tauber, M. E., and Sutton, K., "Stagnation Point Radiative Heating Relations for Earth and Mars Entries," *Journal of Spacecraft and Rockets*, Vol. 28, No. 1, 1991, pp. 40–42.

[30]Seiff, A., Tillman, J. E., Murphy, J. R., Schofield, J. T., Crisp, D., Barnes, J. R., LaBaw, C., Mahoney, C., Mihalov, J. D., Wilson, G. R., and Haberle, R., "The Atmosphere Structure and Meteorology Instrument on the Mars Pathfinder Lander," *Journal of Geophysical Research*, Vol. 102, No. E2, 1997, pp. 4045–4056.

[31]"Entry Data Analysis for Vikings 1 and 2: Final Report," Martin Marietta, Rept. TN-3770218, Denver, CO, Nov. 1976.

R. D. Braun
Guest Editor